

Using a cohesive damage model to predict the tensile behaviour of CFRP single-strap repairs

R.D.S.G. Campilho, M.F.S.F. de Moura, J.J.M.S. Domingues

Abstract

This work addresses both experimental and numerical analyses regarding the tensile behaviour of CFRP single-strap repairs. Two fundamental geometrical parameters were studied: overlap length and patch thickness. The numerical model used ABAQUS® software and a developed cohesive mixed-mode damage model adequate for ductile adhesives, and implemented within interface finite elements. Stress analyses and strength predictions were carried out. Experimental and numerical comparisons were performed on failure modes, failure load and equivalent stiffness of the repair. Good correlation was found between experimental and numerical results, showing that the proposed model can be successfully applied to bonded joints or repairs.

Keywords: Adhesive joints; Composites; Repair; Cohesive damage model

1. Introduction

In the last years carbon-fibre reinforced composites have been widely used for structural applications such as aeronautical, automotive and others, where high performance materials are necessary and recommended. These composite structures are prone to suffer damage, namely delamination between layers. This phenomenon can highly reduce the strength of these structures which, associated to the recycling difficulties and replacement costs, makes repairing very advantageous. Adhesively bonded repairs of structures can offer substantial benefits relatively to the mechanical fastening method, including no significant weight increase, more uniform stress distributions, minimal shape change and reduction of the maintenance costs. The most used methods to adhesively bond damaged structures consist of single or double-lap/strap, scarf and step configurations. Single and double-strap repairs present the advantages of easy execution and low costs. However, for high responsibility or highly stressed structures they are not advisable, as a full strength recovery is not usually achieved. This can be explained by a smaller bond length, compared with scarf repairs, and major stress concentrations due to load eccentricity. In the last years the research on composites repair has increased. In this context, cohesive damage models are accepted instruments to simulate damage onset and growth.

Several studies have been published regarding the applicability of these models to bonded and repaired joints. Works including triangular shape models applied to bonded joints or repairs were considered in the past (de Moura et al., 1997; Chen, 2002; Campilho et al., 2005; Valoroso and Champaney, 2006; Campilho et al., 2007). However, when ductile adhesives are used, it is more adequate to employ trapezoidal softening laws including the plastic behaviour of the adhesive. Regarding these types of laws, one of the first studies included a mixed-mode embedded-process-zone (EPZ) model (Tvergaard and Hutchinson, 1993; Tvergaard and Hutchinson, 1996) to study interfacial fracture of bi-material systems. This involved a three-parameter traction–separation law with the opening and shear stresses and displacements being interdependent in such a way that the intrinsic toughness of the interface is mode-independent. However, the experimental results of Yang et al. (1999) and Yang et al. (2001) showed a significant difference between the values of the toughnesses for the two modes; this indicated that a mode-independent model is not always appropriate for the adhesive system being studied. Yang et al. (1999) used an EPZ model to study the coupling between interface fracture and plastic strain of the adherends. For the adhesive, a traction–separation law including plasticity was used. The model was validated performing T-peel tests on adhesively bonded cracked aluminium double cantilever beams. The same authors (Yang et al., 2001) considered the same traction–separation law for elastic-plastic mode-II crack growth modelling. End-Notched Flexure (ENF) specimens subjected to a bending load, and undergoing extensive plastic strain accompanying failure, were used to validate the model. The main fracture parameters were determined comparing numerical and experimental results for one particular geometry, and then applied to another geometry. The proposed traction–separation law was found appropriate for the particular thickness of the commercial adhesive used and the particular strain rate of the specimens considered. Yang and Thouless (2001) simulated the mixed-mode fracture of plastically deforming adhesive joints using a mode-dependent EPZ. Mode-I and mode-II fracture laws obtained from previous works (Yang et al., 1999; Yang et al., 2001) were combined with a mixed-mode failure criterion to provide quantitative predictions of the deformation and fracture of T-peel specimens and single-lap shear joints. The linear energetic failure criterion was used to establish the separation of the EPZ elements. A linear toughness based criterion (Hutchinson and Suo, 1992) was used to assess complete failure of the EPZ elements and subsequent crack growth. Kafkalidis and Thouless (2002) performed a numerical analysis of single-lap shear joints using a cohesive-zone approach that included the plastic strain of the adhesive. The cohesive-zone model allowed not only the influence of the geometry to be considered, but also included in the analysis the cohesive properties of the interface and plastic deformation of the adherends. Considering cohesive-zone parameters determined for the particular combination of materials used, the numerical predictions showed excellent agreement with the experimental observations. The traction–separation law, failure criterion and model parameters are consistent with Yang and Thouless (2001). Li et al. (2005a) used a cohesive-zone model previously developed by Li et al. (2005b) on adhesively bonded joints to validate both two and three parameter laws. Using this method, the strengths and deformations were accurately described, as well as the transition between failure of the composite and failure of the interface. The Compact-Tension test was used to determine the properties of the traction–separation laws. The results obtained with the three-parameter cohesive-zone model presented a good agreement with the experimental data. Thouless et al. (2006) used a cohesive-zone approach to model the mixed-mode fracture of adhesive GFRP single-lap joints. Accounting for the traction–separation laws, a three parameter law was considered for mode-I (Li et al., 2005a), and a two-parameter law was used for mode-II (Yang and Thouless, 2001). The three-parameter mode-I traction–separation law was used in order to simulate interfacial cracking followed by fibre pull-out (experimentally observed for mode-I fracture). On the other hand, preliminary mode-II tests indicated that only few fibres were pulled out during mode-II fracture. Consequently, a simple two parameter traction–separation law was chosen to simulate the elastic/plastic behaviour of the adhesive for the mode-II debonding process. Experimental and numerical curves revealed excellent agreement, including both the strengths of the joints and the failure mechanisms.

This work presents an experimental and numerical study concerning the tensile behaviour of CFRP single-strap repairs. The failure mode, failure load and stiffness of the repairs were considered. The comparison was

performed for different values of overlap lengths and patch thicknesses. A high resistant adhesive that undergoes extensive plastic strain before failure was used. In order to account for this behaviour, a new cohesive mixed-mode damage model adequate for ductile adhesives was developed. A previous stress analysis was performed to identify the critical regions of the repaired structure, leading to damage initiation. Subsequently, the cohesive damage model is used to predict the failure modes and repair strengths. The results were compared with the experimental ones.

2. Cohesive damage model

2.1. Model description

A cohesive mixed-mode (I + II) damage model based on interface finite elements was developed to simulate damage onset and growth. The objective is to replace the usual solid elements of the adhesive layer. To simulate the behaviour of ductile adhesives, a trapezoidal softening law between stresses (σ) and relative displacements (δ_r) between homologous points of the interface elements with zero thickness was employed (Fig. 1). These types of laws accurately reproduce the behaviour of thin adhesive layers in mode I (Andersson and Stigh, 2004) and mode II (Leffler et al., 2007). The constitutive relationship before damage onset is

$$\sigma = E\delta_r \quad (1)$$

where E is a stiffness diagonal matrix containing the stiffness parameters e_i ($i = I, II$) defined later in this work. Considering the pure-mode model, after $\delta_{1,i}$ (the first inflexion point, which leads to the plateau region of the trapezoidal law) the material softens progressively or, in other words, undergoes damage. This is simulated by the energy being released in a cohesive zone behind the crack tip. This region, known as Fracture Process Zone, is where the material undergoes softening damage by different ways, e.g., microscopic cracks and extensive plasticity. Numerically, this is implemented by a damage parameter whose values vary from zero (undamaged) to unity (complete loss of stiffness) as the material deteriorates. The softening relationship can be written as

$$\sigma = (I - D)E\delta_r \quad (2)$$

where I is the identity matrix and D is a diagonal matrix containing, on the position corresponding to mode i ($i = I, II$) the damage parameter. In the plateau region the damage parameter can be defined as

$$d_i = 1 - \frac{\delta_{1,i}}{\delta_i} \quad (3)$$

and, in the stress softening part of the curve

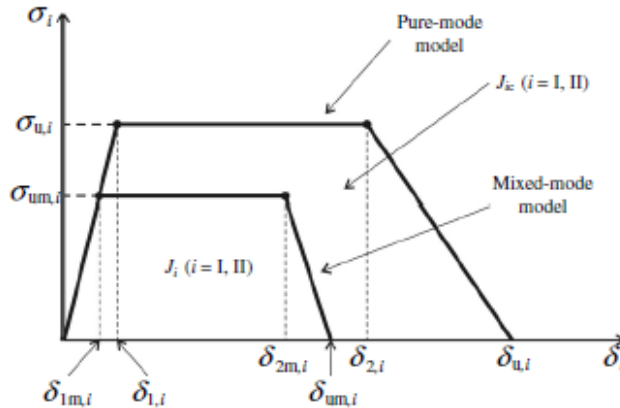


Fig. 1. The trapezoidal softening law for pure-mode and mixed-mode.

$$d_i = 1 - \frac{\delta_{1,i}(\delta_{u,i} - \delta_i)}{\delta_i(\delta_{u,i} - \delta_{2,i})} \quad (4)$$

where d_i is the current relative displacement and $d_{2,i}$ is the second inflexion point of the trapezoidal law, both in each mode ($i = I, II$). The maximum relative displacement, $d_{u,i}$, at which complete failure occurs, is obtained by equating the area under the softening curve to J_{ic} , which corresponds to the respective critical fracture energy

$$J_{ic} = \frac{\sigma_{u,i}}{2}(\delta_{2,i} - \delta_{1,i} + \delta_{u,i}) \quad (5)$$

where $r_{u,i}$ represents the local strength in each mode ($i = I, II$). In general, bonded joints or repairs are subjected to mixed-mode loading. Therefore, a formulation for interface finite elements should include a mixed-mode damage model, which is an extension of the described pure-mode model (Fig. 1). Damage onset is predicted using a quadratic stress criterion

$$\begin{aligned} \left(\frac{\sigma_I}{\sigma_{u,I}}\right)^2 + \left(\frac{\sigma_{II}}{\sigma_{u,II}}\right)^2 &= 1 \quad \text{if } \sigma_I > 0 \\ \sigma_{II} &= \sigma_{u,II} \quad \text{if } \sigma_I \leq 0 \end{aligned} \quad (6)$$

where r_i ($i = I, II$) represent the stresses in each mode. It is assumed that normal compressive stresses do not induce damage. Considering Eq. (1), the first Eq. (6) can be rewritten as function of the relative displacements

$$\left(\frac{\delta_{1m,I}}{\delta_{1,I}}\right)^2 + \left(\frac{\delta_{1m,II}}{\delta_{1,II}}\right)^2 = 1 \quad (7)$$

where $d_{1m,i}$ ($i = I, II$) are the relative displacements in each mode corresponding to damage initiation. Defining an equivalent mixed-mode displacement

$$\delta_m = \sqrt{\delta_I^2 + \delta_{II}^2} \quad (8)$$

and mixed-mode ratio ($i = I, II$)

$$\beta_i = \frac{\delta_i}{\delta_I} \quad (9)$$

the mixed-mode relative displacement at the onset of the softening process (d_{1m}) can be obtained combining Eqs. (7)–(9)

$$\delta_{1m} = \delta_{1,I}\delta_{1,II}\sqrt{\frac{1 + \beta_{II}^2}{\delta_{1,II}^2 + \beta_{II}^2\delta_{1,I}^2}} \quad (10)$$

The corresponding relative displacement for each mode ($d_{1m,i}$) can be obtained from Eqs. (8)–(10)

$$\delta_{1m,i} = \frac{\beta_i \delta_{1,I}\delta_{1,II}}{\sqrt{\delta_{1,II}^2 + \beta_{II}^2\delta_{1,I}^2}} \quad (11)$$

Stress softening onset ($d_{2,i}$) was predicted using a quadratic relative displacements criterion similar to Eq. (7), leading to

$$\left(\frac{\delta_{2m,I}}{\delta_{2,I}}\right)^2 + \left(\frac{\delta_{2m,II}}{\delta_{2,II}}\right)^2 = 1 \quad (12)$$

where $d_{2m,i}$ ($i = I, II$) are the relative displacements in each mode corresponding to stress softening onset. Using a procedure similar to the one followed for d_{1m} , the mixed-mode relative displacement at the onset of the stress softening process (d_{2m}) can be obtained

$$\delta_{2m} = \delta_{2,I}\delta_{2,II}\sqrt{\frac{1 + \beta_{II}^2}{\delta_{2,II}^2 + \beta_{II}^2\delta_{2,I}^2}} \quad (13)$$

The corresponding relative displacement for each mode ($d_{2m,i}$) can thus be obtained

$$\delta_{2m,i} = \frac{\beta_i \delta_{2,I} \delta_{2,II}}{\sqrt{\delta_{2,II}^2 + \beta_{II}^2 \delta_{2,I}^2}} \quad (14)$$

Crack growth was simulated by the linear fracture energetic criterion

$$\frac{J_I}{J_{Ic}} + \frac{J_{II}}{J_{IIc}} = 1 \quad (15)$$

When Eq. (15) is satisfied damage growth occurs and stresses are completely released, with the exception of normal compressive ones. The energy released in each mode at complete failure (J_i , $i = I, II$) can be obtained from the area of the minor trapezoid of Fig. 1

$$J_i = \frac{\sigma_{um,i}}{2} (\delta_{2m,i} - \delta_{1m,i} + \delta_{um,i}) \quad (16)$$

Combining Eqs. (5), (16) and (15) the ultimate mixed-mode relative displacement (d_{um}) can be written as

$$\delta_{um} = \frac{2J_{Ic}J_{IIc}(1 + \beta_{II}^2) - \delta_{1m}(\delta_{2m} - \delta_{1m})(e_I J_{IIc} + \beta_{II}^2 e_{II} J_{Ic})}{\delta_{1m}(e_I J_{IIc} + \beta_{II}^2 e_{II} J_{Ic})} \quad (17)$$

The corresponding relative displacement for each mode ($d_{um,i}$) can be obtained from Eqs. (8), (9) and (17)

$$\delta_{um,i} = \beta_i \frac{2J_{Ic}J_{IIc}(1 + \beta_{II}^2) - \delta_{1m}(\delta_{2m} - \delta_{1m})(e_I J_{IIc} + \beta_{II}^2 e_{II} J_{Ic})}{\delta_{1m}\sqrt{1 + \beta_{II}^2}(e_I J_{IIc} + \beta_{II}^2 e_{II} J_{Ic})} \quad (18)$$

The equivalent quantities d_{1m} , d_{2m} and d_{um} are then used in Eqs. (3) and (4) in order to define the damage parameters.

2.2. Cohesive parameters

The interface finite elements simulating the adhesive layer are intended to replace the solid elements habitually used to model the adhesive. Thus, they incorporate a characteristic length h , which corresponds to the thickness of the adhesive. The stiffness matrix (E) components (e_i , $i = I, II$) are thus obtained from the ratio between the elastic modulus of the material in tension or shear (E or G , respectively) and h . Consequently, the remaining parameters necessary to define the trapezoidal law are the local strengths ($r_{u,i}$), the second inflexion points ($d_{2,i}$) and the fracture energies (J_{Ic}). It is known that the adhesive as a thin layer behaves differently in comparison to the adhesive as a bulk material. Andersson and Stigh (2004) used an inverse method to obtain the cohesive properties of an adhesive layer in mode I using the DCB test. The authors concluded that the local strength in mode I ($r_{u,I}$) is of the same order of magnitude of the tensile strength measured in bulk tests. However, they also concluded that this statement is not valid concerning the fracture strain of the adhesive. On the other hand, Yang et al. (1999) demonstrated, after a series of analyses, that the parameters $d_{1,i}$ and $d_{2,i}$ do not significantly influence the numerical results. Therefore, in the present work, $r_{u,i}$ and $d_{2,i}$ were obtained from the r - e curve of the bulk adhesive (Fig. 2), assumed to be elastic-perfectly plastic. The adhesive used was Araldite® 420, whose properties are listed in Table 1. $r_{u,I}$ was defined as the bulk strength of the adhesive and $d_{2,I}$ was calculated from the product of fracture strain and adhesive thickness. The first inflexion point ($d_{1,I}$) was defined from the initial stiffness of the adhesive in tension and the local strength in mode I ($r_{u,I}$). $r_{u,II}$ was obtained from $r_{u,I}$ and considering the von Mises yield criterion. Owing to its less influence on the results (Yang et al., 1999), $d_{2,II}$ was defined considering that stress softening occurs under a slope similar to the mode I case (Carlberger and Stigh, 2007). On the other hand, it is known that the length of the damage zone, which is intrinsically associated to the plateau size in the trapezoidal law, is substantially larger in shear than in peel (Andersson and Biel, 2006), which supports this choice. Furthermore, a sensitivity analysis is presented in Section 6.3 to study the influence of $d_{2,i}$ of the adhesive on the failure path and load. The critical fracture energies

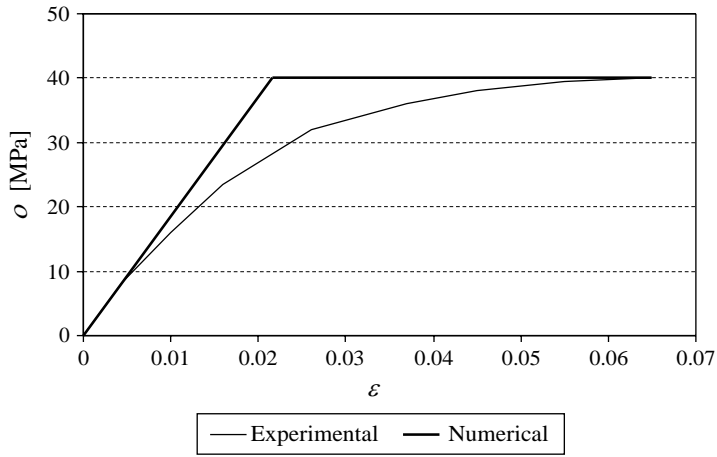


Fig. 2. Stress–strain relationship of the adhesive Araldite® 420 and numerical approximation.

Table 1
Cohesive properties used to simulate different failure modes

	Intralaminar	Adhesive	Fibre
J_{Ic} (N/mm)	0.33	0.6	0.43
J_{IIc} (N/mm)	0.66	1.2	0.66
$r_{u,I}$ (MPa)	32	40	750
$r_{u,II}$ (MPa)	18.5	23.1	23.1
$d_{2,I}$ (mm)	–	0.013	–
$d_{2,II}$ (mm)	–	0.052	–
E (MPa)	–	1850	–
m	–	0.3	–
h (mm)	–	0.2	–

(J_{Ic}) were obtained from Double Cantilever Beam (DCB) and End Notched Flexure (ENF) tests for pure modes I and II, respectively.

The cohesive laws used for intralaminar and fibre failures do not include a plateau as a brittle behaviour is observed. The initial stiffnesses are equated to a quite high value (10^6 N/mm³) and a traditional penalty function method is used (de Moura et al., 1997). The values of intralaminar local strengths and critical fracture energies were obtained in previous works (Campilho et al., 2005; Campilho et al., 2007).

In the particular case of fibre properties, it was verified that the local strength in mode I ($r_{u,I}$) has a significant influence on the crack onset locus. Its value was not experimentally measured. It was determined using an inverse method. A sensitivity analysis is presented in Section 6.3 to study the influence of this parameter on the failure path and load. The critical fracture energy in mode I (J_{Ic}) was established to promote immediate failure after $r_{u,I}$ is reached, since the composite has a brittle behaviour under mode I in the fibres direction.

3. Experimental work

The geometry of the single-strap specimens is presented in Fig. 3. The parent laminates and patches were manufactured considering unidirectional 0° lay-ups of carbon/epoxy prepreg (TEXIPREG HS 160 RM) with 0.15 mm of ply thickness, whose mechanical properties are presented in Table 2 (Campilho et al., 2005). Curing was achieved in a press for 2 h at 130 °C and 2 bar pressure. The bonding process included roughening the surfaces to be bonded with sandpaper and cleaning with compressed air to increase the adhesion and avoid adhesive failure, followed by assembly and holding with contact pressure and curing at room temperature. General initial dimensions of the repairs are presented in Table 3. Overlap lengths of 5, 10, 15 and 20 mm were considered. Patch thicknesses of 0.6, 1.2, 1.8 and 2.4 mm were also evaluated. Table 4 presents the different

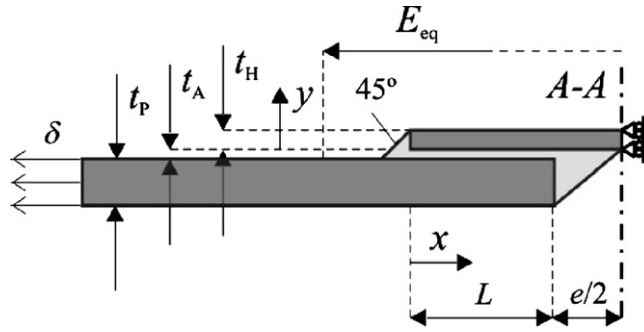


Fig. 3. Single-strap repair geometry.

Table 2

Parent laminates and patches mechanical properties

Parent laminates and patches mechanical properties		
$E_1 = 1.09 \times 10^5$ MPa	$m_{12} = 0.342$	$G_{12} = 4315$ MPa
$E_2 = 8819$ MPa	$m_{13} = 0.342$	$G_{13} = 4315$ MPa
$E_3 = 8819$ MPa	$m_{23} = 0.380$	$G_{23} = 3200$ MPa
r_u of a 0° layer: 750 MPa		

Table 3

Parent laminates, patches and adhesive dimensions

Parent laminates	Patches	Adhesive
Width: $b = 15$ mm	Thickness: $t_H = 1.2$ mm	Thickness: $t_A = 0.2$ mm
Thickness: $t_P = 2.4$ mm	Overlap length: $L = 15$ mm	
Spacing between laminates: $e = 5$ mm		

Table 4

Different geometries and types of failure observed

Specimen	L (mm)	t_H (mm)	Failure type
S1	5	1.2	A
S2	10	1.2	A
S3	15	1.2	A
S4	20	1.2	A
S5	15	0.6	A
S6	15	1.2	A
S7	15	1.8	A
S8	15	2.4	B

values of L and t_H used, as well as the experimental and numerical failure types observed (to be characterized later in this work). Three specimens were considered for each geometry. Adhesive fillets at the edges of the overlap were used for all geometries, comprising all the parent laminate and patch thicknesses (see Fig. 3 for shape and dimensions). The use of adhesive fillets is widely considered to increase the efficiency of bonded joints, as peel stresses are reduced (Kim et al., 2006; Rispler et al., 2000). The specimens were tested under a tensile loading using an INSTRON testing machine at room temperature under displacement control. Experimental setup is presented in Fig. 4. Strains were measured using a 55 mm characteristic length strain gauge. The loading rate was kept constant at 0.5 mm/min.

Intralaminar failures in the parent laminate and patch were observed experimentally. These occurred at an average distance of 0.05 mm from the parent laminate/adhesive and patch/adhesive interfaces. The failure mechanisms will be discussed in more detail in Section 5.

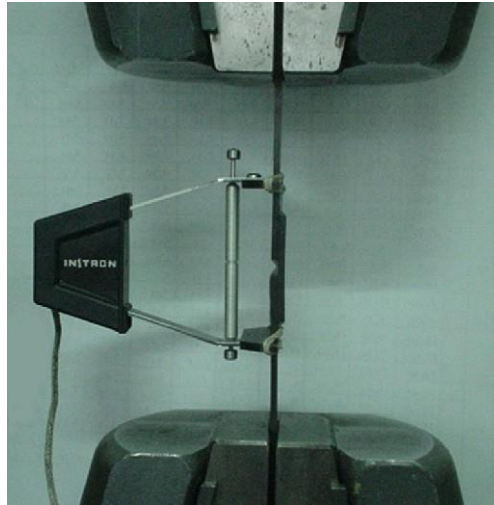


Fig. 4. Experimental setup in the testing machine.

4. Numerical analysis

A non-linear material and geometrical numerical analysis was performed, using plane stress 8-node rectangular and 6-node triangular finite solid elements available in the ABAQUS[®] library. Fig. 5 shows a detail of the used mesh at the overlap region. Eight layers of elements were used through thickness for the parent laminates and the patches. Symmetry conditions were used at the middle of the repair (line A-A in Fig. 3) and a tensile displacement was applied at the edge of the model. The interface finite elements were placed at several locations in the model (Fig. 6) to simulate crack onset and growth, in order to account for different failure modes. These included failure in the adhesive (line P2) and intralaminar failures of the parent laminate (line P1) or patch (line P3). In view of the possible failure modes likely to occur (intralaminar, in the adhesive and fibre rupture), three different sets of cohesive properties were considered (Table 1 and Fig. 7). Three locations of possible fibre rupture were considered (Fig. 6): in the parent laminate at the outer edge of the overlap, in the patch at the inner edge of the overlap, and in the patch at the symmetry line A-A (thick marks in Fig. 6). The position of these elements allowed several options for damage onset (locations 1, 2, 3 and 4 in Fig. 6), damage growth (lines P1, P2 and P3 in Fig. 6) and final failure (locations 5, 6, 7 and 8 in Fig. 6). Vertical interface elements allow fillets separation from the parent laminate and patch (respectively locations 4 and 8 in Fig. 6), as well as an alteration of the crack growth path between lines P1, P2 and P3 at the inner and outer edges of the overlap.

5. Failure modes

The first comparison between the experimental work and the numerical analysis concerns the failure modes. Experimentally, two distinct ones were observed: type A and type B. Type A failure represents an intralaminar

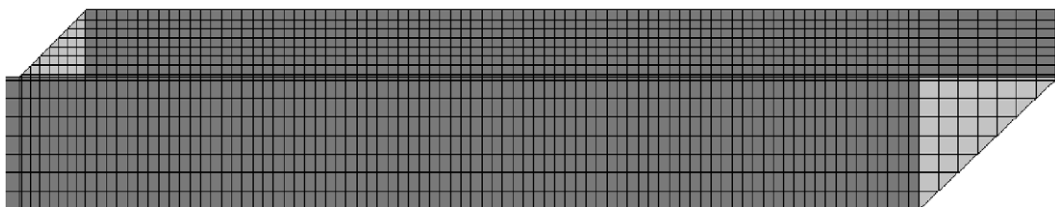


Fig. 5. Detail of the mesh for geometry S3.

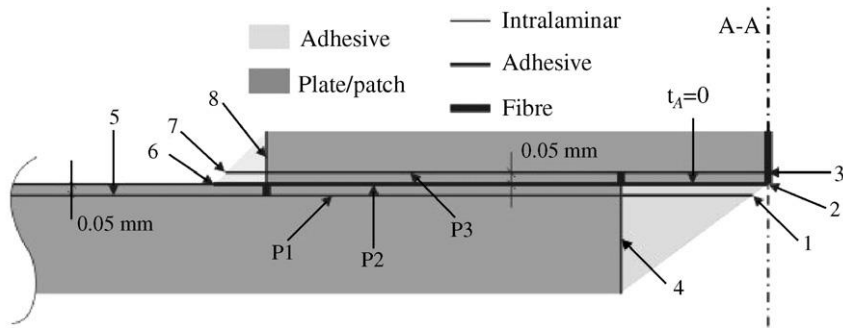


Fig. 6. Location of the interface finite elements.

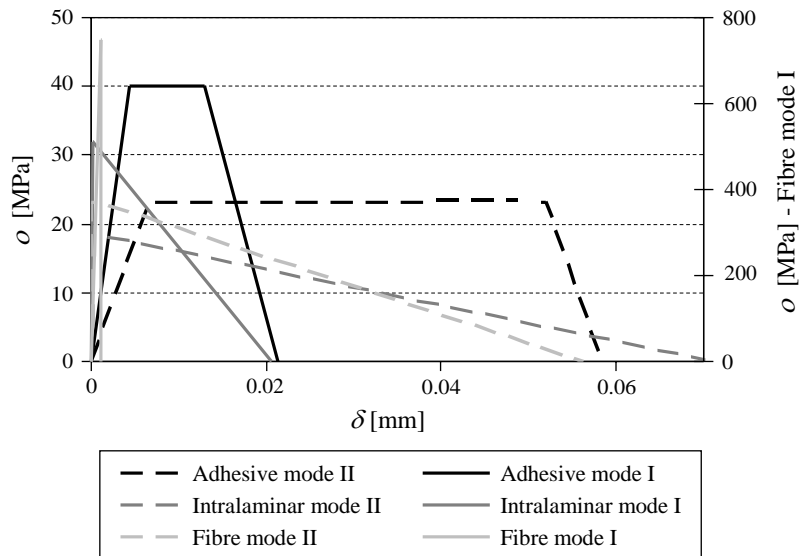


Fig. 7. Cohesive softening laws used.

failure of the patch (Fig. 8 a). Failure initiates with fibre rupture at line A-A between locations 2 and 3 and then crack grows along line P3 (Fig. 6), while the inner fillet remains intact. Type B failure is a combination of intralaminar failure of the parent laminate and patch (Fig. 8b). In this situation, failure onset occurs within the

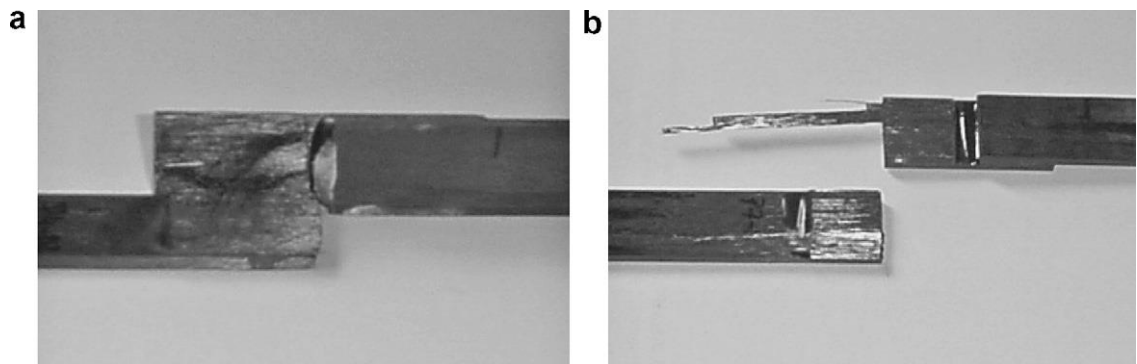


Fig. 8. Type A (a) and type B (b) final failures obtained experimentally.

inner fillet, with no patch fibres rupture (location 1 in Fig. 6), and then grows as an intralaminar failure of the parent laminate and patch along lines P1 and P3. Final failure occurs at the outer edge of the overlap, namely at the outer fillet/patch vertical interface (location 8 in Fig. 6) for type A and B failures. Type B failure was observed only for all S8 specimens ($t_H = 2.4$ mm). Type A failure was observed for all specimens of the remaining geometries (S1–S7).

The mentioned crack onset locations and subsequent growth paths until complete laminate/patch separation were captured by the numerical simulations. In fact, models ranging from S1 to S7 presented a type A failure, while model S8 presented a failure similar to type B already described, with intralaminar failure only of the patch. However, before failure, both interfaces P1 and P3 presented similar magnitude of the stresses in the respective interface elements, proving that both failures are prone to occur. Fig. 9a represents the numerical type A crack onset for geometry S3. Damage initiates with fibres rupture at line A–A between locations 2 and 3 (Fig. 6). Subsequently, crack grows along line P3. Fig. 9b shows the numerical type B crack onset for geometry S8. Crack initiation occurs at location 1, propagating as an intralaminar patch failure along line P3. Type A and B numerical final failures are presented in Fig. 10a and b, respectively, for the same geometries. In both situations, damage grows along line P3 from the inner edge to the outer edge of the overlap. Complete separation at the outer fillet/patch vertical interface (location 8) is observed for type A and B failures. These numerical results are consistent with the experimentally obtained crack onset locations and growth paths until complete failure.

Fig. 11 presents the cross-sectional tensile stresses (σ_x) in the patch at the symmetry line A–A for each patch thickness, normalized by the average stress in the patch at line A–A for geometry S3 (σ_{avg}). Type A failure onset characterized by fibres rupture at line A–A is justified by the high stiffness of the composite along the fibres directions, associated with the patch bending. These phenomena cause significant tensile stresses in the fibre representative interface elements located between locations 2 and 3 (Fig. 6), high enough to induce patch fibres failure prior to failure in the adhesive. The modification of the failure mode for the highest value of patch thickness is related to the reduction of the maximum tensile stresses in the patch at the symmetry line A–A. In fact, as the patch thickness increases, the applied load is distributed by a larger area. For the specimens with 2.4 mm patch thickness, the maximum tensile stresses are not enough to induce fibres rupture in the patch and the damage starts within the inner adhesive fillet (location 1 in Fig. 6).

6. Results

6.1. Stress analysis

A stress analysis in the elastic region was conducted to better understand the influence of shear and peel stresses on the repair crack onset location and to justify the regions where the interface finite elements were placed. In all cases stresses are normalized by σ_{avg} , the average shear stress along the overlap for geometry

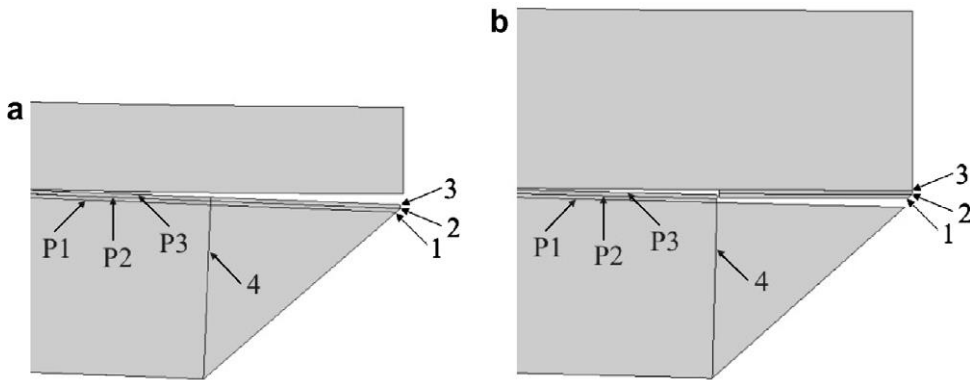


Fig. 9. Type A (a) and type B (b) crack initiation locations obtained numerically.

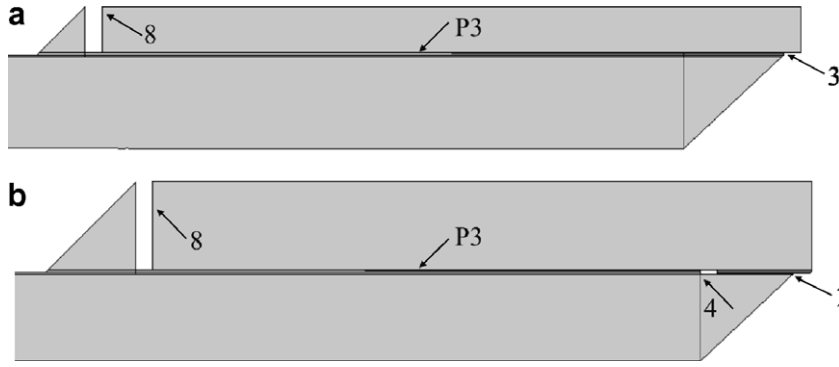


Fig. 10. Type A (a) and type B (b) final failures obtained numerically.

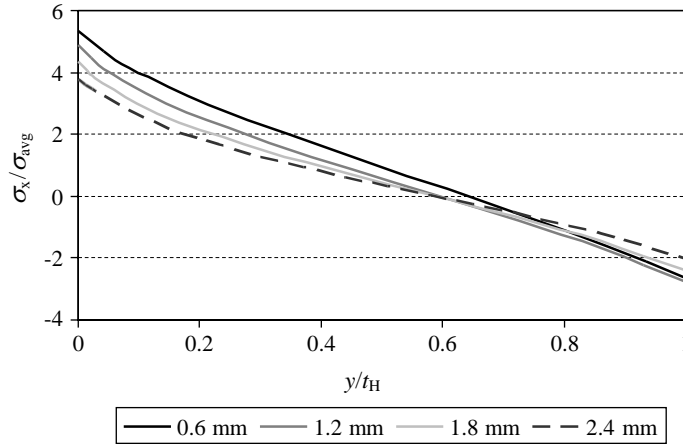


Fig. 11. Normal stresses along line A-A as function of the patch thickness.

S3 at location P2 (Fig. 6). Two additional failure loci, corresponding to the interlaminar region between the two layers of the parent laminate and patch closest to the adhesive (lines L1 and L2), were considered in the stress analysis. These failure paths are placed at 0.15 mm from the adhesive and were included to justify the option of using interface finite elements at 0.05 mm from the adhesive (intralaminar failures experimentally observed).

Figs. 12 and 13 present the shear and peel stresses, respectively, for geometry S3 at lines L1, P1, P2, P3 and L2. Typical profiles for these kinds of joints (Campilho et al., 2005; Cognard et al., 2006; Kilic et al., 2006) were obtained in this work. It is stressed that shear stresses at locations L1 and L2 are remarkably lower at the crack onset region (inner edge of the overlap and symmetry line A-A), comparing with locations P1 and P2. Moreover, shear stresses at locations L1 and L2 at the symmetry line A-A are practically null. Thus, locations L1 and L2 were not considered as critical failure regions and, consequently, interface finite elements were not used at those locations.

6.2. Stiffness and failure load

The proposed model was also validated with failure load and stiffness analyses of the repairs, both as functions of the values of L and t_H presented in Table 4. Numerical and experimental P - d curves for geometry S5 are presented in Fig. 14. A good agreement was found, in terms of stiffness and failure load/displacement. Experimental and numerical stiffnesses (E_{eq}) and failure loads (F) of the repairs were compared. E_{eq} denotes for the equivalent stiffness of the repair along 55 mm at the repair region (see Fig. 3 for clarity). This length

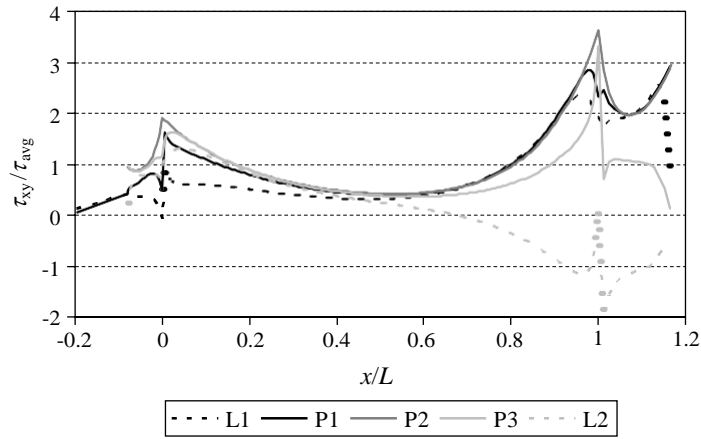


Fig. 12. Shear stresses at locations L1, P1, P2, P3 and L2 for geometry S3.

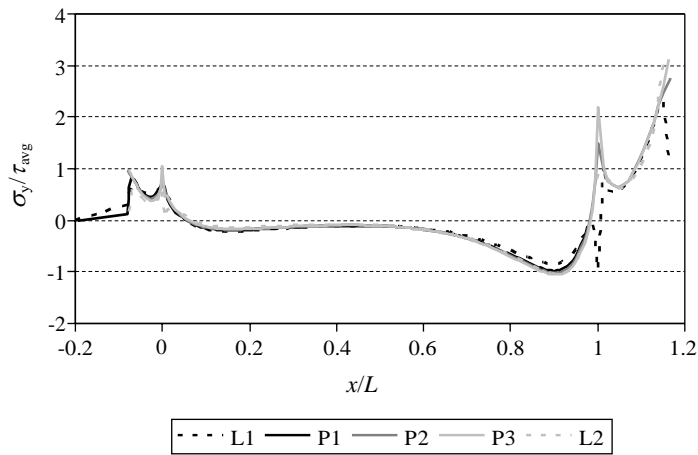


Fig. 13. Peel stresses at locations L1, P1, P2, P3 and L2 for geometry S3.

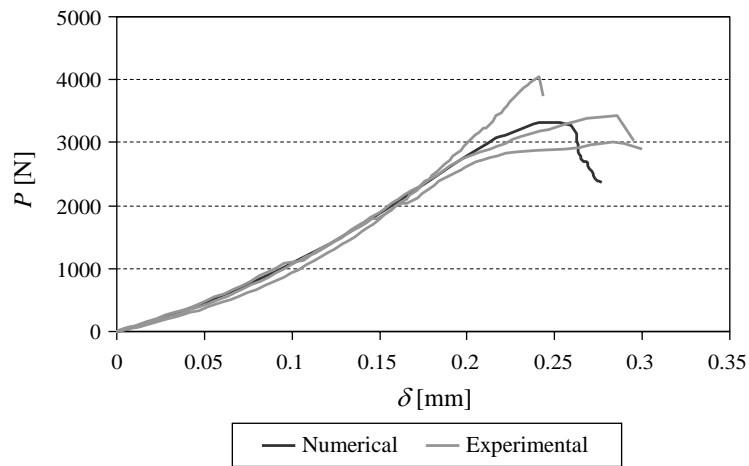


Fig. 14. Numerical and experimental P - d curves for geometry S5.

represents the effective span of the strain gauge used (Fig. 4) and is considered as an approximation of the repair stiffness. F represents the maximum load sustained by the specimens. Figs. 15 and 16 show E_{eq} and F , respectively, as functions of the overlap length. Figs. 17 and 18 present the same quantities, as functions of the patch thickness. The standard deviation of the experimental results is included in the graphs. The numerical results in Fig. 15 show a slight increasing trend of E_{eq} as function of L , which is not clearly observed in the experiments. This is probably due to small variations of the adhesive thickness, once the repair stiffness depends markedly on the adhesive deformation. Fig. 16 shows a good agreement between numerical and experimental maximum loads as function of L . It is observed that F is an approximately linear function of the overlap length (Campilho et al., 2005; Hu and Soutis, 2000). The increase of the adhesive resistant shear area justifies this behaviour, although the shear stress distributions are generally more favourable for the lowest values of L (Campilho et al., 2005).

The influence of the patch thickness on E_{eq} (Fig. 17) is noticeable, as higher values of t_H lead to stiffer repairs. This is explained by the reduction of the repair rotation with thicker patches. Fig. 18 shows a slight reduction of F when the patch thickness increases from 0.6 to 1.2 mm, and an increase from that point. This reduction of failure load for the lower values of t_H is explained by the increase of both peak peel and shear stresses near the inner region of the overlap (Campilho et al., 2005). However, from $t_H = 1.2$ mm this effect is overcome by the reduction of the repair bending which induces delay of the fibre or fillet adhesive initial rupture, causing an increase of the failure load. For $t_H = 2.4$ mm, the alteration of the failure mode also justifies the load increase for this geometry. The observed behaviour is related to the intralaminar failures. Using weaker adhesives, a failure in the adhesive region is expected, with F decreasing with the patch thickness (Campilho et al., 2005; Hu and Soutis, 2000), and it is not observed the increasing trend for the highest values of t_H . Generally, experimental and numerical results present a good agreement.

6.3. Sensitivity analyses

Sensitivity analyses were performed on the cohesive parameters which play a significant role in the failure process and were not measured by specific experimental tests.

A study was conducted, considering geometry S3, to assess the influence of $d_{2,i}$ of the adhesive on the failure path and load, considering its range of possible values (from 0%, corresponding to $d_{2,i} = d_{1,i}$ and a triangular law, to 100%, corresponding to $d_{2,i} = d_{u,II}$ and an abrupt failure when $d_{2,i}$ is reached). This study was accomplished for $d_{2,I}$ and $d_{2,II}$ separately and simultaneously (using the same percentile range of values). No difference was observed in the failure mode originally observed, as well as the repair failure loads, which can be justified by the intralaminar failures observed.

The influence of intralaminar mode I (J_{Ic} and $r_{u,I}$), mode II (J_{IIc} and $r_{u,II}$) and overall (J_{Ic} , $r_{u,I}$, J_{IIc} and $r_{u,II}$) properties on failure path and load was also analysed. Values ranging from -50% to $+50\%$ of the initial ones considered in this analysis (Table 1) were considered. Fig. 19 presents the failure load as function of the

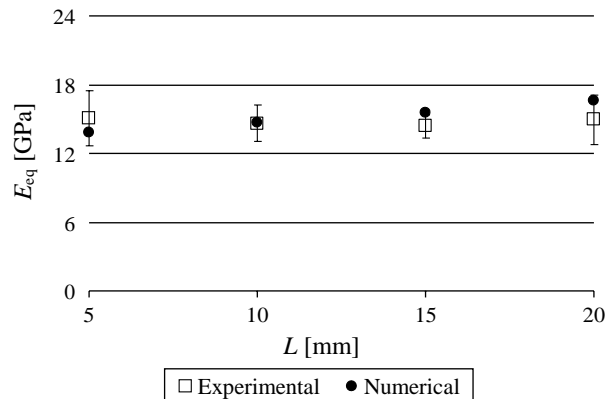


Fig. 15. Equivalent stiffness as function of the overlap length.

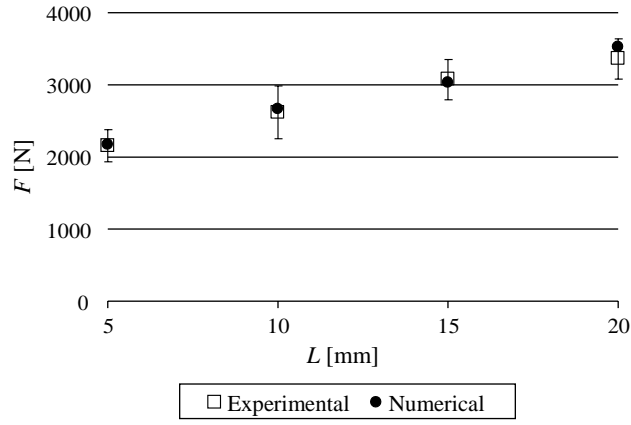


Fig. 16. Failure load as function of the overlap length.

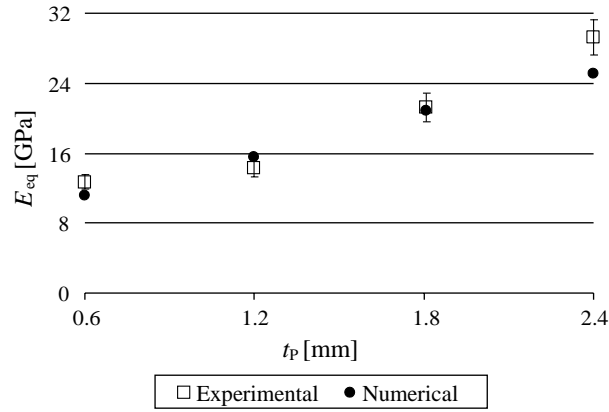


Fig. 17. Equivalent stiffness as function of the patch thickness.

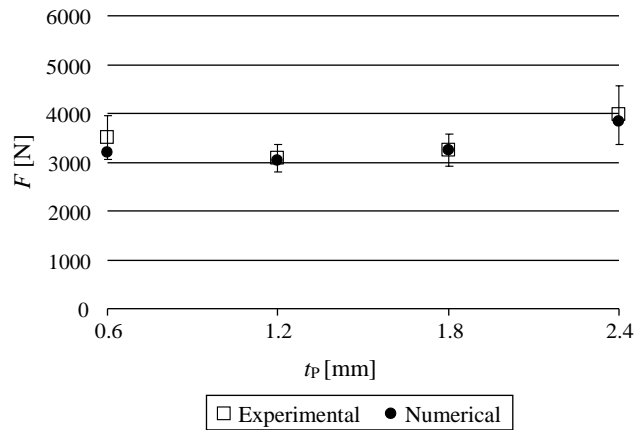


Fig. 18. Failure load as function of the patch thickness.

intralaminar properties. These failure loads are normalized by the failure load of the geometry S3 repair using the initial properties (F_0). Overall, the failure load increases with each group of properties considered in this study. As expected, mode II properties have a higher effect on the failure load, since the repair is primarily

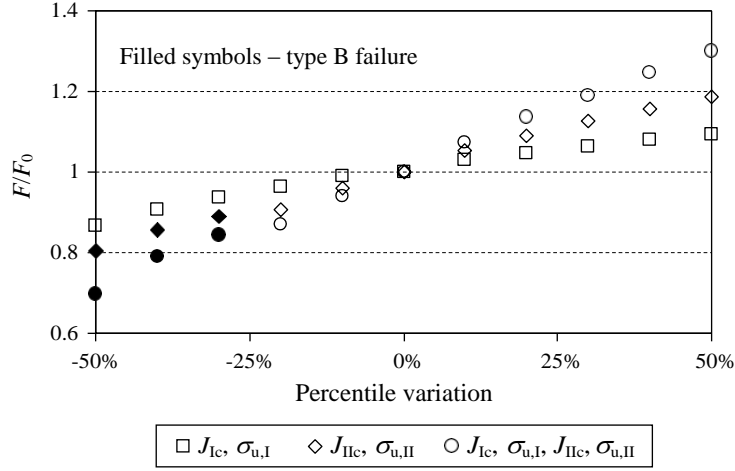


Fig. 19. Failure load as function of the intralaminar properties.

loaded in shear. Concerning the failure modes, a modification to type B was observed reducing 30% or more mode II and overall properties (filled symbols in Fig. 19). This modification is justified by the strength reduction at line P1, causing premature failure at that location, before the local strength in the fibre interface elements at line A–A is reached.

In the case of fibre failure the local strength in mode I ($r_{u,I}$) is the most important parameter relating to crack onset. An analysis was conducted for $r_{u,I}$ ranging between 500 and 1000 MPa in order to evaluate its influence on the failure path and load. A type A failure was observed for all geometries using $500 \text{ MPa} < r_{u,I} < 710 \text{ MPa}$. In this case, the lower values used for $r_{u,I}$ lead to fibre failure at locations 2 and 3 (Fig. 6) prior to damage initiation and growth at location 1 for all geometries. In the interval of $710 \text{ MPa} < r_{u,I} < 792 \text{ MPa}$ a type B failure was observed only for geometry S8, as occurred experimentally. This modification was caused by the increase of $r_{u,I}$ for the fibre interface elements at locations 2 and 3 (Fig. 6), leading to damage initiation at location 1 for geometry S8 before the local strength in mode I is reached and the respective failure for the fibre interface elements occurs. Between $792 \text{ MPa} < r_{u,I} < 827 \text{ MPa}$, a type B failure was also observed for geometry S7, which was not observed experimentally. For $r_{u,I} > 827 \text{ MPa}$, the other geometries also present a type B failure, which does not correspond to the experimental observations. Consequently, an average value of the interval $710 \text{ MPa} < r_{u,I} < 792 \text{ MPa}$ was selected (750 MPa). In the range of $r_{u,I}$ values studied, no difference was observed in the failure load.

7. Concluding remarks

The objective of this work was to validate a developed mixed-mode cohesive damage model in order to simulate crack onset and growth in structural repairs executed with ductile adhesives. The model was applied on tensile loaded single-strap CFRP repairs, for different overlap lengths and patch thicknesses. A stress analysis was performed in order to identify critical regions of damage onset and growth. The model performance was evaluated by comparing numerical results with experiments, in terms of equivalent stiffness and failure load of the repairs, as well as the failure path observed. A slight increase of the equivalent stiffness as function of the overlap length was numerically obtained, although no definitive conclusions could be drawn from the experimental results. The equivalent stiffness increased with the patch thickness. Strength predictions were very accurate. The failure load increases with the overlap length. On the other hand, a gradual reduction of the failure load was observed with the increase of the patch thickness, for the smallest patch thicknesses. For the highest patch thicknesses an increase was observed, due to the diminishing of the rotation of the repair and to the alteration of the failure mode. The reduction of the failure load for the lowest values of patch thicknesses was explained by the increase of the peel and shear stress peaks located at the inner edge of the overlap, where crack initiates. The experimentally observed failure modes were also reproduced in the numerical

analysis, in terms of failure onset and progression path until failure. The authors thereby conclude that the presented model can be successfully applied to predict failure load and path for these kinds of repairs, when using ductile adhesives.

Acknowledgements

The authors thank the Portuguese Foundation for Science and Technology for supporting the work here presented, through the research project POCI/EME/56567/2004 and the individual grant SFRH/BD/30305/2006.

References

- Andersson, T., Biel, A., 2006. On the effective constitutive properties of a thin adhesive layer loaded in peel. *International Journal of Fracture* 141, 227–246.
- Andersson, T., Stigh, U., 2004. The stress-elongation relation for an adhesive layer loaded in peel using equilibrium of energetic forces. *International Journal of Solids and Structures* 41, 413–434.
- Campilho, R.D.S.G., de Moura, M.F.S.F., Domingues, J.J.M.S., 2005. Modelling single and double-lap repairs on composite materials. *Journal of Composites Science and Technology* 65, 1948–1958.
- Campilho, R.D.S.G., de Moura, M.F.S.F., Domingues, J.J.M.S., 2007. Stress and failure analyses of scarf repaired CFRP laminates using a cohesive damage model. *Journal of Adhesion Science and Technology* 21, 855–870.
- Carlberger, T., Stigh, U., 2007. An explicit FE-model of impact fracture in an adhesive joint. *Engineering Fracture Mechanics* 74, 2247–2262.
- Chen, J., 2002. Predicting progressive delamination of stiffened fibre-composite panel and by decohesion models. *Journal of Thermoplastic Composite Materials* 15, 429–441.
- Cognard, J.Y., Davies, P., Sohier, L., Créac'hcadec, R., 2006. A study of the non-linear behaviour of adhesively-bonded composite assemblies. *Composite Structures* 76, 34–46.
- de Moura, M.F.S.F., Gonçalves, J.P.M., Marques, A.T., de Castro, P.M.S.T., 1997. Modeling compression failure after low velocity impact on laminated composites using interface elements. *Journal of Composite Materials* 31, 1462–1479.
- Hu, F.Z., Soutis, C., 2000. Strength prediction of patch repaired CFRP laminates loaded in compression. *Composites Science and Technology* 60, 1103–1114.
- Hutchinson, J.W., Suo, Z., 1992. Mixed mode cracking in layered materials. *Advances in Applied Mechanics* 29, 63–191.
- Kafkalidis, M.S., Thouless, M.D., 2002. The effects of geometry and material properties on the fracture of single lap-shear joints. *International Journal of Solids and Structures* 39, 4367–4383.
- Kilic, B., Madenci, E., Ambur, D.R., 2006. Influence of adhesive spew in bonded single-lap joints. *Engineering Fracture Mechanics* 73, 1472–1490.
- Kim, K.S., Yoo, J.S., Yi, Y.M., Kim, C.G., 2006. Failure mode and strength of uni-directional composite single lap bonded joints with different bonding methods. *Composite Structures* 75, 192–198.
- Leffler, K., Alfredsson, K.S., Stigh, U., 2007. Shear behaviour of adhesive layers. *International Journal of Solids and Structures* 44, 530–545.
- Li, S., Thouless, M.D., Waas, A.M., Schroeder, J.A., Zavattieri, P.D., 2005a. Use of mode-I cohesive-zone models to describe the fracture of an adhesively-bonded polymer-matrix composite. *Journal of Composites Science and Technology* 65, 281–293.
- Li, S., Thouless, M.D., Waas, A.M., Schroeder, J.A., Zavattieri, P.D., 2005b. Use of a cohesive-zone model to analyze the fracture of a fiber reinforced polymer-matrix composite. *Journal of Composites Science and Technology* 65, 537–549.
- Rispler, A.R., Tong, L., Steven, G.P., Wisnom, M.R., 2000. Shape optimization of adhesive fillets. *International Journal of Adhesion & Adhesives* 20, 221–231.
- Thouless, M.D., Waas, A.M., Schroeder, J.A., Zavattieri, P.D., 2006. Mixed-mode cohesive-zone models for fracture of an adhesively bonded polymer-matrix composite. *Engineering Fracture Mechanics* 73, 64–78.
- Tvergaard, V., Hutchinson, J.W., 1993. The influence of plasticity on the mixed-mode interface toughness. *Journal of the Mechanics and Physics of Solids* 41, 1119–1135.
- Tvergaard, V., Hutchinson, J.W., 1996. On the toughness of ductile adhesive joints. *Journal of the Mechanics and Physics of Solids* 44, 789–800.
- Valoroso, N., Champaney, L., 2006. A damage-mechanics-based approach for modelling decohesion in adhesively bonded assemblies. *Engineering Fracture Mechanics* 73, 2774–2801.
- Yang, Q.D., Thouless, M.D., Ward, S.M., 1999. Numerical simulations of adhesively-bonded beams failing with extensive plastic deformation. *Journal of the Mechanics and Physics of Solids* 47 (6), 1337–1353.
- Yang, Q.D., Thouless, M.D., Ward, S.M., 2001. Elastic-plastic mode-II fracture of adhesive joints. *International Journal of Solids and Structures* 38, 3251–3262.
- Yang, Q.D., Thouless, M.D., 2001. Mixed-mode fracture analyses of plastically deforming adhesive joints. *International Journal of Fracture* 110, 175–187.